Dissolution Rates of Amorphous Al- and Fe-Phosphates and their Relevance to Phosphate Mobility on Mars

Revision 1

V. M. Tu[1]

E.M. Hausrath.[1,*]

O. Tschauner [1,2]

V.Iota[2]

G.W. Egeland [3]

[1] Department of Geoscience, University of Nevada, Las Vegas, 4505 S. Maryland Parkway, Las Vegas, NV 89154 USA, elisabeth.hausrath@unlv.edu

[2] HiPSEC, University of Nevada Las Vegas, 4505 S Maryland Parkway, Las Vegas, Nevada, USA

[3] Department of Mechanical Engineering, University of Nevada, Las Vegas, 4505 S. Maryland Parkway, Las Vegas, NV 89154 USA

* to whom correspondence should be addressed: Elisabeth M. Hausrath Department of Goscience, University of Nevada, Las Vegas, 4505 S. Maryland Parkway, Las Vegas, Nevada 89154 (702) 895-1134 (phone) 702-895-4064 (fax) Elisabeth.Hausrath@unlv.edu

Abstract

Phosphate is an essential element for life on Earth, and therefore if life exists or ever existed on Mars it may have required phosphate. Amorphous Al- and Fe-phosphates rapidly precipitate

from acidic solutions and amorphous Al-phosphates likely control phosphate concentrations in some natural waters on Earth. The amorphous fraction of martian soils has also been shown to be enriched in P, and amorphous phosphates are therefore also likely important in the phosphate cycle on Mars. Despite this importance, however, few dissolution rates exist for amorphous Al- and Fe- phosphates. In this study, dissolution rates of amorphous Al- and Fe-phosphates were measured in flow-through reactors from steady state concentrations of Al, Fe and P. A pH – dependent rate law, $\log R = \log k - npH$ was determined from the dissolution rates, where R is the dissolution rate, k is the intrinsic rate constant and n is the reaction order with respect to H^+. For amorphous Al-phosphate, $\log k = -6.539 \pm 1.529$, and $n = 2.391 \pm 0.493$. For amorphous Fe-phosphate, $\log k = -13.031 \pm 0.558$, and $n = 1.376 \pm 0.221$. The amorphous Al-phosphate dissolves stoichiometrically under all experimental conditions measured, and the amorphous Fe-phosphate dissolves non-stoichiometrically, approaching stoichiometric dissolution as pH decreases, due potentially to Fe oxyhydroxides precipitating and armoring grain surfaces. Perhaps due to these effects, amorphous Al-phosphate dissolution rates are approximately three orders of magnitude faster than the amorphous Fe-phosphate dissolution rates measured under these experimental conditions. Amorphous Al-phosphate dissolution rates measured in this study are also faster than published dissolution rates for the crystalline Al-phosphate variscite. The rapid dissolution rates of amorphous Al- and Fe-phosphates measured in this study therefore suggest that, if these phases are present on Mars, phosphate would be rapidly released into acidic environments.

Keywords: phosphate, Mars, mineral dissolution, kinetics, habitability, astrobiology, amorphous phases, synchotron

Introduction

Phosphate is an essential nutrient for life on Earth, and its release and mobility is therefore important to assessing potential habitability on Mars. The primary phosphate minerals present in martian meteorites include Cl-bearing apatite and merrillite, and recent work has indicated that release of P from these minerals is higher than that from the dominant terrestrial P-bearing mineral, fluorapatite, with important implications for P availability on Mars [Adcock et al. 2013]. Recent results from the Mars Science Laboratory Curiosity indicate that the amorphous fraction of martian soils is enriched in P [Morris et al., 2013; Vaniman et al. 2014], and phosphate release from amorphous phosphate phases may therefore also be important in interpreting phosphate availability on Mars.

Previous work has shown that amorphous P-bearing phases are likely important in terrestrial environments. Roncal-Herrero et al. [2009] report that the first phosphate-containing phases to precipitate from super-saturated acidic fluids in laboratory experiments are amorphous Al- and Fe-phosphates. In long term (up to 5 years) laboratory experiments designed to test whether amorphous Al phosphates eventually become the crystalline Al-phosphate variscite after prolonged aging, Hsu [1982a] concluded that amorphous Al-phosphates, not variscite, are the likely products of phosphate fertilizers in acidic terrestrial soils. Similar long-term aging experiments of amorphous Fe-phosphates indicated that they were unlikely to recrystallize to the crystalline Fe-phosphate strengite for up to 66 months [Hsu 1982b]. Analyses of terrestrial natural waters also indicate that Al and phosphate concentrations are consistent with control by equilibrium with either variscite or amorphous Al-phosphate under acidic conditions [Roncal-Herrero and Oelkers 2011], and sequential-fractionation data from extraction analyses of

cultivated sandy soils from citrus groves in Florida suggest that amorphous Al- and Fe-phosphates and P associated with crystalline Al- and Fe-oxides account for a significant portion of the total P [Zhang et al., 2001]. These results all suggest that amorphous Al and Fe-phosphates are important on Earth, and potentially also on Mars.

P may also be present sorbed to surfaces in the amorphous martian material. The lack of correlation between phosphorous concentrations and nanophase oxides in dusts measured by the Mars Exploration Rovers indicate that sorbed phosphate may not be the dominant phase in Martian soils [Morris et al., 2006], however other work suggests sorbed phosphates may be present [Barger-Rampe and Morris, 2012].

Amorphous phosphates are therefore likely important phases on Mars. Despite their potential importance, however, few experiments have examined the dissolution rates of and phosphate release from amorphous phosphate-containing phases [Huffman, 1960]. In this study, we measure the dissolution rates of and phosphate release from amorphous Al- and Fe-phosphates, to shed light on potential phosphate mobility on Mars.

Methods

Materials:

Amorphous Al- and Fe-phosphates were synthesized in batch reactors after Roncal-Herrero et al. [2009], except that syntheses were performed at 50°C for 24 hours, continuously shaken at 100 strokes per minute and larger volumes were used to yield sufficient mass for dissolution experiments. The use of synthetic materials was chosen to ensure consistent, pure phases for reproducible results in dissolution experiments. Preliminary syntheses were performed for 12, 24, and 48 hour durations, and the material synthesized for 24 hours was chosen for dissolution experiments because particles had coalesced to a more solid mass, but no evidence of

crystallinity was detected by powder diffraction (Appendix Figure 1a-b). In all cases, solutions were made with 18.2 M Ω deionized water and high purity chemicals. Aqueous solutions (0.1M Al- or Fe-$(NO_3)_3$, and 0.1M KH_2PO_4 and 0.09M KOH) were preheated to 50°C, combined while continuously stirring and immediately sealed and immersed in the 50°C shaking water bath. Batches were cooled to 25° C after 24 hours, and the slurry centrifuged at 9860 rpm for 2-10 minutes until supernatants were clear. Supernatants were decanted, and solid phases washed 3 times with 18.2 M Ω deionized water and air dried at room temperature for 2-5 days.

Experimental Setup:

In order to determine dissolution rates under Mars-relevant acidic conditions, dissolution experiments of amorphous Al- and Fe-phosphates at pH values of 1, 2, 2.5 and 3 were conducted using flow-through reactors based on those used by Weissbart and Rimstidt [2000] (Figure 1). Samples were sieved to 75-150µm particle size, and 1.000 to 3.000 ± 0.004 g was placed on a 0.45µm acrylic membrane filter held in place with an acrylic sleeve within the reactor, with the reactor already filled with solution to prevent the formation of bubbles. The input solution consisted of a 0.01M KNO_3 solution adjusted to the pH of the experiment (1, 2, 2.5, or 3) with high purity 1 N HCl and 1 N NaOH. Solution was pumped up through the filter using a VWR variable-speed ultra low-flow peristaltic feed pump, and the reactor was continuously agitated on a shaker plate at 150 rpm. Uncertainty on flow-rates for pump 1 is ± 0.029 ml/min and for pump 2 is ± 0.048 ml/min (one standard deviation). The outlet solution was filtered through a 0.45µm filter before entering the collection vessel, and concentrations were measured until steady state was obtained, defined as at least four consecutive data points of pH values that did not vary more than ± 0.1 units, flow rates that did not vary more than ± 0.05 ml/min, and concentrations that did not vary by more than 10%. In one experiment (pH =

2.5), the reactor was perturbed, affecting the solution concentrations (Appendix Table 2). Concentrations at saturation of Fe, Al and P were also measured either in a batch reactor (Al-phosphate) or a flow-through reactor with the flow rate stopped (Fe-phosphate) after ~ 2 weeks (Appendix Table 17).

Analyses:

Outlet solutions were collected at predetermined intervals based on preliminary experiments, weighed for flow rate determination, and measured for pH using a SevenEasy Mettler Toledo AG pH probe. Separate aliquots were re-filtered through 0.45µm filters, acidified to below pH 2 using 1 N high purity HCl for preservation, and stored at 4°C until chemical analysis.

Aluminum concentrations were measured by the catechol violet colorimetric method [Dougan and Wilson, 1974] at a wavelength of 585 nm, and phosphate concentrations were determined by the molybdate blue colorimetric method [Murphy and Riley, 1962] at a wavelength of 882 nm on a Thermo Scientific Genesys 10S UV-Vis Spectrophotometer. Flame Atomic Absorption Spectroscopy (AAS) was used to measure Fe concentrations on a Thermo Scientific iCE 3000 series AA spectrometer. The uncertainty (one standard deviation) on analyses is as follows: for Fe concentrations the uncertainty is ± 0.0164 ppm , and for Al and P (as phosphate) ± 0.0435 ppm. Uncertainty on analyses was estimated by repeated measurements of standards and blanks, based on modified methods from Perkin-Elmer [1964]. The method uncertainty is documented as ± 0.19 ppm for Fe [Greenberg et al., 2005], ± 2% for Al [Dougan and Wilson 1974], and ± 8% for P as phosphate [Murphy and Riley 1962].

Powders were analyzed by X-ray diffraction (XRD) and indicate amorphous material (Appendix Figures 1a-b). Analyses were completed using a PANalytical X'PERT Pro X-ray

Diffraction Spectrometer and Cu Kα radiation (λ = 1.5406 Å) with data collected every 0.02 degrees 2θ at 20 mA and 40kV from 5 to 75 degrees 2θ with a step size of 0.08° in the X-ray Diffraction and X-ray Fluorescence Laboratory (XXL) at UNLV. Powdered samples of amorphous Al- and Fe-phosphates were gold coated and observed using a JEOL JSM-6700F Field Emission Scanning Electron Microscope (FE-SEM) at working distances of 8.0mm to 8.4mm at 2.0 or 5.0kV in Secondary Electron Imaging mode (SEI) and a Scanning Electron Microscope (SEM) (JEOL ASM-5600), at a working distance of 20mm and accelerating voltage of 15kV, with a spot-size of 20 and using Energy Dispersive Spectroscopy (EDS) for composition determination in the Electron Microanalysis and Imaging Laboratory (EMIL) at UNLV. Surface areas were determined using a Micromeritics ASAP 2020 Gas Sorption Analyzer using N_2 and are 121.9128 ± 0.4702 (m^2/g) (amorphous Fe-phosphate) and 77.155 ± 0.3943 (m^2/g) (amorphous Al-phosphate). In order to help interpret changes to the material with reaction, both unreacted amorphous Fe phosphates, and amorphous Fe phosphates reacted at pH = 2.5 (from the end of the experiment) were vacuum-impregnated with epoxy, polished with 18.2 M Ω deionized water using 1μm grit diamond lapping paper, and examined both optically and by SEM-EDS (JEOL ASM-5600) at a working distance of 20mm and accelerating voltage of 10kV, with a spot-size of 40 in SEI and using EDS for composition.

Unreacted and reacted iron phosphate material (pH = 3) was further analyzed by synchrotron microXRD, and XANES, and reacted material (pH = 3) by TEM. Synchrotron diffraction was conducted with high energy and with 10^4 times higher flux than in-house X-ray sources in order to a) examine the amorphous diffraction signal of reacted and unreacted Fe-phosphate over an extended Q-range and b) search for possible very small amounts of crystalline phases in these materials. The synchrotron diffraction experiments were conducted at the

163 superconducting bending magnet beamline 12.2.2 ALS with a 25 keV primary beam focused to
164 12x15 μm^2 at sample position. The diffraction signal was collected with a MAR 345 image plate
165 detector after 30 min of signal accumulation. Dark-colored reaction rims, μm-scale opaque
166 inclusions, and the less strongly colored core regions of reacted samples were all examined. In
167 addition, unreacted pristine Fe-phosphate was examined. In all cases, absorbance of the X-ray
168 beam by the specimens was less than 10% and no changes of the diffraction signal were
169 observed over time.

170 The TEM SAED analysis was conducted in order to identify nano-crystalline phases. High
171 resolution transmission electron microscopy (HRTEM) data were obtained using a Tecnai G^2
172 F30 S-Twin TEM instrument operated at 200 kV using a field emission gun in Schottky mode as
173 an electron source at UNLV.

174 The XANES spectra were collected in transmission geometry using 0.8eV resolution
175 monochromated beam at sector 12.2.2 at the Advanced Light Source at Berkeley National
176 Laboratory. Both the reacted and unreacted samples were ground using mortar and pestle into a
177 fine powder, and subsequently filtered through a 3 μm Whatman filter. The resulting powder
178 specimens were contained between 0.5mill Kapton foil and placed in a holder on an X-Y
179 scanning stage. The synchrotron beam was focused onto a 100μm spot on the sample using a pair
180 of Kirkpatrick Baez X-ray mirrors. Several spectra were collected at various XY coordinates on
181 each specimen to check for consistency and sample uniformity. XANES spectra were collected
182 in a 500eV window bracketing the Fe Ke-edge transition (7112eV). The resulting spectra were
183 normalized to the size of the edge jump to ensure an accurate comparison across all specimens.
184
185

Calculations

Dissolution rate calculation:

Dissolution rates were calculated from steady state Al, Fe and P concentrations and flow rates normalized to BET surface area [White and Brantley, 1995]:

$$R = \frac{(C_{out} - C_{in})Q}{A \cdot m} \qquad \textbf{(Eq. 1)}$$

where C_{out} is the measured steady state output concentration (mM), C_{in} is the input concentration (mM) (assumed to be zero based on below detection measurements of all method blanks), Q is the flow rate (L/s), A is the specific surface area (cm^2/g), and m is the mass (g). Rates were normalized to final, assumed to be steady state, masses, multiplied by the specific surface area.

Rate laws:

Rate laws were established for amorphous Al- and Fe-phosphate dissolution by applying linear regression analysis to the log dissolution rates versus pH values from each experiment. The pH dependence of dissolution of amorphous Al- and Fe-phosphate is fit to the following equation: $\log R = \log k - n\text{pH}$, where R is the dissolution rate, k is the intrinsic rate constant and n is the reaction order with respect to H^+. For amorphous Al-phosphate, $\log k = -6.539 \pm 1.529$, and $n = 2.391 \pm 0.493$. For amorphous Fe-phosphate, $\log k = -13.031 \pm 0.558$, and $n = 1.376 \pm 0.221$. Values were calculated based on 3 pH values in our experiments, 2, 2.5 and 3 because the material completely dissolved in the pH=1 experiment. The larger reaction order with respect to H^+ for Al versus Fe is consistent with the following dissolution equations:

$$AlPO_4 \cdot xH_2O + 2H^+ \rightarrow Al^{3+} + H_2PO_4^- + xH_2O \qquad \textbf{(Eq. 2)}$$

208 $$FePO_4 \cdot xH_2O + H^+ \rightarrow Fe(OH)^{2+} + H_2PO_4^- + (x-1)H_2O \qquad \textbf{(Eq. 3)}$$

209 *Saturation indices:*

210 Saturation indices were calculated for each steady state condition using PhreeqC
211 [Parkhurst and Appelo, 1999], for strengite, variscite, goethite, hematite, maghemite, vivianite,
212 ferrihydrite, 10nm goethite, 10nm maghemite, 10nm hematite, and gibbsite using values from
213 [Parkhurst and Appelo, 1999; Roncal-Herrero and Oelkers, 2011; Elwood-Madden et al., 2012]
214 (Table 3). Due to the uncertainties in the solubilities of amorphous Al- and Fe-phosphates
215 [Roncal-Herrero and Oelkers, 2011] saturation indices were not calculated for the amorphous
216 Al- and Fe-phosphates. However, our stopped-flow and batch experiments, which show higher
217 concentrations than the steady state concentrations from our flow through reactors at the same
218 pH, indicate that the experimental conditions are undersaturated with respect to these phases,
219 consistent with their dissolution.

220 **Results**

221 *Solution pH:*

222 Output solution pH values typically displayed one of two behaviors, with either constant
223 pH values throughout the experiment, or increasing from low initial pH values to steady state
224 values (Figure 2b, Tables 1-2, Appendix Tables 1-8).

225 *Concentrations:*

226 Fe and Al concentrations typically display one of two behaviors, either remaining steady
227 throughout the entire experiment, or decreasing from initially higher concentrations to reach
228 steady values (Figure 2c, Tables 1-2, Appendix Tables 1-8). Phosphorus concentrations
229 generally decreased over time in all experiments (Figure 2d, Tables 1-2, Appendix Tables 1-8).

230 *Stoichiometry of Release***:**

Steady-state dissolution of amorphous Fe-phosphate was non-stoichiometric in all cases, but steady-state dissolution approached stoichiometric dissolution as pH decreased (Figure 3). In contrast, steady-state amorphous Al-phosphate dissolution was stoichiometric in all experiments (Figure 4). The fluctuation in non-stoichiometric dissolution observed in the amorphous Fe-phosphate pH = 2.5 experiment is attributed to the perturbation of the reactor during this period of time.

Saturation state of steady state solutions:

Saturation indices determined using PhreeqC [Parkhurst and Appelo, 1999] indicate that steady state solutions were undersaturated with respect to all Fe-bearing secondary phases tested (Tables 4-5). Saturation indices for Al-phosphate experiments indicate that solutions are undersaturated with respect to gibbsite, and over-saturated with respect to the crystalline Al-phosphate variscite, which is not surprising for dissolution of an amorphous phase with the same chemical composition.

Reacted Material Characterization:

Reacted and unreacted amorphous Al- and Fe-phosphates were imaged by FE-SEM and indicate a consistent decrease in the size of the globules for Al-phosphates, and a variable decrease in the size of the globules for Fe-phosphates (Figures 5a-d and 6a-d) after reaction. Unreacted amorphous Al-phosphate has globule sizes of ~ 45 to 64nm in diameter, and unreacted amorphous Fe-phosphate globule sizes of ~ 26 to 100nm in diameter. Reacted amorphous Al-phosphate material has slightly smaller diameters than that of unreacted material (~ 27 to 33 nm) (Figures 5a-c), and reacted Fe-phosphate material varied from globule sizes that were comparable to unreacted to slightly smaller globule sizes.

Optical analyses of reacted and unreacted amorphous iron-phosphate material indicate that the unreacted material is a translucent, reddish color, with few, small dark inclusions (Figure 7 c and d). In contrast, the reacted material has an opaque, whitish interior, with darker red rims (Figures 7 a and b). In order to interpret these optical changes, we further analyzed the reacted amorphous Fe phosphates using Synchotron microXRD analysis, TEM and X-ray Absorption Near Edge Structure (XANES) analysis. Synchotron microXRD indicates that the structure of the amorphous reacted and unreacted iron-phosphate is indistinguishable down to ≥ 0.8 Å (Fig 8). However, the unreacted phosphate contained ~ 0.1 % of micro-crystalline phases which could be interpreted as belonging to goethite and bernalite (Figure 8, insert). This small amount of crystalline material was not detected by in-house powder diffraction. In Figure 8, insert, the diffractogram of reacted phosphate was subtracted from the diffractogram of unreacted phosphate, thus removing most of the amorphous diffraction signal for the unreacted material. The micro-crystalline diffraction features are clearly visible. We show the calculated diffraction patterns of goethite and bernalite for comparison. We note that with increasing angle the signal is somewhat suppressed as consequence of the diffraction image processing and calculated and observed intensities do not fully match.

It is somewhat surprising that the reacted phosphate does not contain these crystalline phases. Therefore, we examined the reacted material with XANES and HRTEM and found, by TEM, small nano-crystalline inclusions within an amorphous phosphate matrix. The HRTEM lattice interferences of the nanocrystalline phases were Fourier-transformed and integrated (Ma et al 2011). Although the quality of the electron diffraction pattern suffered from low signal and superimposed amorphous contributions, we tentatively identified strengite and an alkaline-bearing iron oxyhydroxide with structural relation to akaganeite and priderite (Appendix Figure

2). The diffraction signal of nanocrystalline phases generally includes contributions from the crystallite shape. In the case of TEM diffraction data, the structure factors are also affected by the thickness of the sample. These parameters could not be corrected in the present case and are likely to contribute to the differences between the observed and calculated diffraction patterns (Appendix Figure 2).

The XANES spectra show that reacted and unreacted phosphate are very similar (Figure 9). While there is a ~ 10% difference in the intensity of the white line, its position remains unchanged. This is also true of the main edge, which is representing the probability and energy of the Fe 1s $\rightarrow$ 4p and 1s $\rightarrow$ continuum transitions [Deb et al. 2005]. The absence of a shift in the main edge indicates that the valence has remained unchanged during the reaction. The white line energy as well as the energy of the peak at 7136 eV are consistent with literature data for $FePO_4$ [Deb et al 2005]. However, both spectra deviate from the spectrum of pure $FePO_4$ in the noticeably higher relative intensity of the white-line. This higher intensity of the white line has been observed in the triphyllite-$FePO_4$ system and been correlated with octahedrally coordinated Fe^{3+}. The intensity of the pre-edge feature reflects this presence of octahedrally coordinated Fe^{3+}: the pre-edge feature is caused by the forbidden 1s $\rightarrow$ 3d transitions and in cubic crystal field split into two peaks related to transitions into the d-states of e_g and t_{2g} symmetry. In tetrahedral coordination and for ferric Fe the e_g state has lower energy and the pre-edge XANES peak has higher intensity than the t_{2g} related peak. In octahedral coordination it is the opposite. In comparison to crystalline iron phosphate the present two spectra show a higher intensity of the t_{2g}-related feature though less than in triphyllite [Deb et al 2005]. The reacted sample appears to have a slightly smaller ratio t_{2g}/e_g. The energies of the pre-edge features are identical to previous reports [Deb et al. 2005] and do not change after reaction. Hence, there may be a minor decrease

299 in Fe^{3+} in octahedral coordination over Fe^{3+} in tetrahedral coordination which may reflect a
300 gradual progress in crystallization of the amorphous Fe phosphate to strengite. The per-mille-
301 level Fe-oxyhdyroxide phases in reacted and unreacted phosphate do not make noticeable
302 contributions to the XANES spectra due to their very small amount.

303 Thus, it appears that the micro-crystalline iron oxyhydroxides of the unreacted phosphate
304 matrix dissolve or were transformed during reaction, and that a new alkaline-bearing oxy-
305 hydroxide formed, potentially both from the micro-crystalline iron oxyhydroxides, and non-
306 stoichiometric dissolution of the amorphous Fe-phosphate. Iron oxyhydroxides may therefore
307 play an important role in the dissolution processes of iron-phosphates.

308 **Discussion**

309 The amorphous Fe-phosphate dissolution rates from this study were compared to
310 dissolution rates of crystalline and colloidal Fe-phosphates from the literature [Huffman, 1960].
311 Our dissolution rates at pH 2, 2.5, and 3 are slower than the dissolution rates reported at pH 6
312 (Figure 10) possibly due to the much larger surface areas, although since dissolution rates for
313 strengite and colloidal Fe phosphate were not reported for similar experimental conditions at
314 similar pH values, rates are not directly comparable. We compared the amorphous Al-
315 phosphate dissolution rates measured in this study to the dissolution rates of the crystalline Al-
316 phosphate variscite at the same pH, and they are faster (Figure 10). This result is similar to
317 previous studies, which indicate that amorphous silica, for example, dissolves more rapidly than
318 quartz [Liang and Readey, 1987]. Based on these results, therefore, aqueous solutions
319 interacting with amorphous phases are likely to release more phosphate than is released from
320 aqueous interactions with crystalline phosphate phases.

The amorphous Al- and Fe-phosphates used in this study are quite similar. The unreacted amorphous Al- and Fe-phosphates used in this study have similar large surface areas (although the surface area of the Fe phosphate is approximately one and one half times greater than the surface area of Al phosphate), and both consist of nanoporous material as observed by FE-SEM (Figures 5a-d and 6a-d). In addition, although we did not synthesize solid solutions of amorphous Al- and Fe- phosphates, many Al and ferric phosphate phases have complete solid solution including strengite and variscite [Huminicki and Hawthorne, 2002; Taxer and Bartl, 2004] . Despite the similarities between the amorphous phases, however, the dissolution rates measured here are much slower for the amorphous Fe-phosphates than for amorphous Al-phosphates (Figure 10). This result is similar to previous results indicating that strengite dissolves more slowly than variscite at comparable citrate concentrations and pH, with the effect decreasing with increased pH [Malunda, 2000]. Perhaps explaining the difference in dissolution rates between the phases, the dissolution of amorphous Al-phosphate is stoichiometric, whereas the dissolution of the amorphous Fe phosphate is non-stoichiometric (Figures 3 and 4).

Non-stoichiometric dissolution can be due to a number of causes. Common mechanisms identified in the literature consist of the formation of a leached layer and effects of grinding or re-precipitation. Chin and Mills [1991] observed in acidic kaolinite dissolution experiments that sorption and precipitation of silica might cause incongruent dissolution. Cubillas et al. [2005] observed a mineral coating of otavite on $CaCO_3$ in near neutral dissolution experiments, which decreased dissolution rates. Hellmann et al. [2003] proposed an interfacial dissolution-re-precipitation mechanism in labradorite feldspar experiments. Weissbart and Rimstidt [2000] documented, in wollastonite dissolution experiments aimed at improving models of leached

layer formation, the formation of a hydrated silica leached layer influencing the dissolution of wollastonite in solutions with pH ranging from 2 to 6. Putnis [2009] proposed an interface-coupled dissolution precipitation reaction for a variety of minerals including quartz, kaolinite and feldspar. Ruiz-Agudo et al. [2012] utilized Putnis' mechanism in reporting evidence that an amorphous silica leached layer is formed via a tight interface-coupled two-step process: stoichiometric dissolution of mineral surfaces and subsequent precipitation of a secondary phase from a supersaturated boundary layer of fluid in contact with the mineral surface.

In dissolution experiments of Fe-bearing minerals that may be particularly relevant to dissolution of the amorphous Fe-phosphates in our study, poorly crystalline iron oxyhydroxide precipitation may be the controlling factor causing incongruent dissolution. Elwood Madden et al. [2012] observed incongruent jarosite dissolution thought to be dependent on iron oxyhydroxide reaction products formed in solutions at pH > 3.5. Siever and Woodford [1979] described the development of a precipitated poorly crystalline Fe hydroxide layer, armoring mineral surfaces of mafic minerals such as fayalite, hypersthene, basalt and obsidian. Huffman et al. [1960] report incongruent dissolution of strengite and colloidal ferric phosphate in water, similar to our findings. Huffman et al. [1960] also document surface coatings consisting of Fe hydroxides on strengite and colloidal ferric phosphate, which they confirm by microscopic examination. Malunda [2000] also observed non-stoichiometric dissolution of strengite, which they attributed to the formation of a secondary phase or a surface complex of Fe. In Al- and Fe-phosphate precipitation experiments, Hsu [1976] demonstrated rapid formation of Fe-oxides, which they attribute to the much larger first hydrolysis constant for Fe^{3+} of 2.5×10^{-3} [Lamb and Jacques, 1938], compared to the first hydrolysis constant of Al^{3+} (1.05×10^{-5}) [Frink and Peech, 1963]. We therefore postulate that the non-stoichiometric dissolution of amorphous Fe-

367 phosphate and the slow dissolution rates relative to amorphous Al-phosphate observed in these
368 experiments may be due to the re-precipitation of secondary Fe-oxyhydroxide phases, similar to
369 the findings of Huffman [1960], Siever and Woodford [1979], and Elwood-Madden et al.
370 [2012], and due to the much larger first hydrolysis constant for Fe^{3+} than for Al^{3+}.
371 In order to investigate the possible formation of Fe-oxyhydroxides, the saturation state of
372 the output solutions was calculated relative to strengite, goethite, hematite, maghemite,
373 vivianite, ferrihydrite, 10nm goethite, 10nm hematite, and 10nm maghemite. [Parkhurst and
374 Appelo, 1999; Roncal-Herrero and Oelkers, 2011; Elwood-Madden et al., 2012] (Table 4), and
375 was found to be undersaturated with respect to all of these minerals. As described above, the
376 synchrotron micro-XRD and TEM analyses indicate the possible presence of goethite and
377 bernalite in the unreacted amorphous Fe phosphates, and nano-crystalline strengite and an iron
378 oxyhydroxide in the reacted material, with reaction progress towards strengite also indicated by
379 the XANES results. Due to the minimal change between the unreacted and reacted amorphous
380 Fe phosphate observed by synchrotron microXRD (Figure 8) and XANES (Figure 9), and the
381 fact that upon additional heating strengite forms from solutions of the composition used to
382 synthesize these amorphous materials, [Roncal-Herrero et al. 2009], we propose that strengite
383 was not formed during the reaction of our material in our dissolution experiments, but rather
384 was present in the unreacted material.
385 We therefore propose that, upon reaction in our experiments, the trace Fe oxides present in
386 the unreacted material dissolve, perhaps contributing to the formation of the nanocrystalline Fe
387 oxyhydroxide in the reacted material, which is likely also the result of non-stoichiometric
388 dissolution of the amorphous Fe phosphate. This result is consistent with the optical
389 observations, which indicate that the unreacted material is a translucent, reddish material

throughout, with dark inclusions (Figure 7 c and d), presumably the result of the goethite and bernalite, respectively. The reacted material exhibits a whitish interior, with reddish rims (Figures 7 a and b), presumably the result of the dissolution of the goethite and the bernalite from the initial material, and the precipitation of the iron oxyhydroxide in the reddish rim of the reacted material. This result is also consistent with the non-stoichiometric dissolution observed in the solution chemistry, as well as with the results of Ruiz-Agudo et al., [2012], who document the formation of a re-precipitated secondary phase using *in situ* atomic force microscopy (AFM) and FE-SEM despite undersaturation of the bulk solution with respect to secondary phases.

Dissolution rates were measured here in flow-through reactors, which although complicated to run, yield the most easily interpreted data since secondary products do not build up in solution as they do in batch reactors. In this case, an additional possibility is the transport of suspended phases. Although images of unreacted and reacted phases show decreased globular sizes, indicative of dissolution, previous work on natural waters has shown significant transport of trace elements in the colloidal fraction [Dupre et al., 1996; Viers et al., 1997]. Transport by colloids may have occurred as evidenced by the presence of staining on filters, indicative of transport of colloids in solution that were retained on the filters. Colloids retained on the filter would have decreased the measured dissolution rates, and colloids passing through the filter would have increased the rate. Transport of colloidal particles may be an important process under acidic conditions on Mars as well as on Earth.

Implications for Mars

412 Recent work from the MSL Curiosity indicate that the amorphous component of the martian
413 soil is enriched in P [Morris et al. 2013; Vaniman et al. 2014]. Previous terrestrial studies
414 indicate that amorphous phosphates are important in terrestrial processes, and may also be
415 important on Mars [Hsu 1982a, b; Zhang et al. 2001; Roncal-Herrero et al. 2009; Roncal-
416 Herrero and Oelkers 2011]. However, few dissolution rates for amorphous Al- and Fe-
417 phosphates exist in the literature and therefore, determination of dissolution rates and rate laws
418 for these phases are helpful to understanding phosphate mobility on Mars.
419 Amorphous Al-phosphate yields congruent dissolution rates that are faster than its
420 crystalline counterpart, variscite, and than amorphous Fe-phosphate. In contrast, the amorphous
421 Fe-phosphate dissolved incongruently and more slowly than the amorphous Al-phosphate,
422 which may be due to the re-precipitation of a nanocrystalline Fe oxyhydroxide, armoring grain
423 surfaces, and inhibiting dissolution. Rate laws of the form $\log R = \log k - npH$ were calculated
424 from dissolution rates, with values for amorphous Al-phosphate of: $\log k = -6.539 \pm 1.529$, and
425 $n = 2.391 \pm 0.493$ and amorphous Fe-phosphate, $\log k = -13.031 \pm 0.558$, and $n = 1.376 \pm 0.221$.
426 The fast dissolution rates of amorphous Al- and Fe-phosphates indicate rapid release of
427 phosphates into acidic environments, such as those potentially present on Mars, suggesting
428 significant phosphate mobility on that planet.
429 These results may be applicable to environments such as Meridiani Planum, where some
430 have argued for the episodic presence of acidic groundwater [Squyres et al., 2006], as well as
431 Gale Crater, where the P-enriched amorphous phases have been detected [Morris et al., 2013;
432 Vaniman et al. 2014]. The presence of acidic water would facilitate the formation of Al- and Fe
433 phosphates at Meridiani Planum [Roncal-Herrero et al. 2009], and episodic liquid water would
434 tend to favor formation of amorphous rather than crystalline phosphates on Mars [Tosca and

435 Knoll 2009]. Amorphous Al- and Fe-phosphates may therefore be an important phosphate
436 source for environments such as Meridiani Planum and Gale Crater on Mars. We conclude from
437 this study that they are likely to release abundant phosphate into solution, with important
438 implications for potentially habitable environments on Mars.
439

440 **Acknowledgements:**

441 We would like to acknowledge funding from the Mars Fundamental Research Program
442 Grant NNX10AP58G to E. M. Hausrath, Marathon Oil Corporation, the Hispanic
443 Scholarship Fund, the UNLV Geoscience Department, and the Graduate and Professional
444 Students Association. Work was in part supported by the National Nuclear Security
445 Administration under the Stewardship Science Academic Alliances program through DOE
446 Cooperative Agreement #DE-NA0001982. We would additionally like to acknowledge Seth
447 Gainey, Christopher Adcock, Michael Steiner, Renee Schofield, Kirellos Sefein, , Paul Forster,
448 Mingua Ren, Rachael Johnsen, Alastair McDowell, and Brandon Guttery for their contributions
449 to this project. We also appreciate very helpful reviews from 2 anonymous reviewers which
450 greatly strengthened this manuscript. The Advanced Light Source is supported by the Director,
451 Office of Science, Office of Basic Energy Sciences, of the U.S. Department of Energy under
452 Contract No. DE-AC02-05CH11231.
453

454 **References:**
455
456 Adcock, C.T., Hausrath, E.M., and Forster, P.M. (2013) Readily available phosphate from
457 minerals in early aqueous environments on Mars Nature Geoscience, 6, 824-827.
458 Barger-Rampe, E., Morris, R.V. (2012) Detecting Adsorbed Sulfate and Phosphate on
459 Nanophase Weathering Products on Mars. AGU abstract, control ID: 1478172.
460 Chin, P.K. F., and Mills, G.L. (1991) Kinetics and Mechanisms of Kaolinite Dissolution: Effects
461 of Organic Ligands. Chemical Geology, 90, 307-317.

462 Cubillas, P. Kohler, S., Prieto, M., Causserand, C., and Oelkers, E.H. (2005) How do Mineral
463 Coatings Affect Dissolution Rates? An Experimental Study of coupled $CaCO_3$
464 Dissolution- $CdCO_3$ Precipitation. Geochimica et Cosmoshimica Acta, 69, 23, 5459-
465 5476.
466 Deb, A., Bergmann, U., Cramer, S.P., and Cairns, E.J. (2005) Structural investigations of
467 LiFePO4 electrodes and in situ studies by Fe X-ray absorption spectroscopy.
468 Electrochimica Acta, 50(25–26), 5200-5207.
469 Dougan, W.K., and Wilson, A.L. (1974) The Absorptiometric Determination of Aluminium in
470 Water. A Comparison of Some Chromogenic Reagents and the Development of
471 Improved Method: Analyst, 99, 413-430.
472 Dupre´, B., Gaillardet, J., Rousseau, D., and Allegre, C. J. (1996) Major and Trace Elements of
473 River-borne Material: The Congo Basin: Geochimica et Cosmochimica Acta, 60, 1301–
474 1321, doi:10.1016/0016-7037(96)00043-9.
475 Elwood-Madden, M.E., Madden, A.S., Rimstidt, J.D., Zahrai, S., Kendall, M.R., and Miller,
476 M.A. (2012) Jarosite Dissolution Rates and Nanoscale Mineralogy. Geochimica et
477 Cosmoshimica Acta, 91, 306-321.
478 Frink, C.R. and Peech M. (1963) Hydrolysis of the Aluminum Ion in Dilute Aqueous Solutions.
479 Inorg. Chem. 2. 473-478.
480 Greenberg A.E., Eaton, A.D., Lenore, S.C., and Rice, E.W. (2005) Standard Methods for the
481 Examination of Water and Wastewater. Standard Methods 21st ed., 3-17 – 3-18.
482 Hellmann, R., Penisson, J.M., Hervig, R.L., Thomassin, J.H., and Abrioux, M.F. (2003) An
483 EFTEM/HRTEM High-Resolution Study of the Near Surface of Labradorite Feldspar
484 Altered at Acid pH: Evidence for Interfacial Dissolution-Reprecipitation. Phys. Chem.
485 Minerals, 20, 192-197.
486 Hsu, P.H. (1976) Comparison of Iron(III) and Aluminum in Precipitation of Phosphate from
487 Solution. Water Research, 10, 903-907.
488 Hsu, P.H., (1982a) Crystallization of Variscite at Room Temperature. Soil Science, 133, 5.
489 Hsu, P.H., (1982b) Crystallization of Iron(III) Phosphate at Room Temperature. Soil Science
490 Society of America Journal, 46, 5, 928-932.
491 Huffman, E.O. (1960) Rates and Mechanisms of Dissolution of some Ferric Phosphates: Soil
492 Science, 1-8.
493 Huminicki, D. M.C., and Hawthorne, F.C. (2002) The Crystal Chemistry of the Phosphate
494 Minerals. Reviews in Mineralogy and Geochemistry, 48.1, 123-253.
495 Lamb A.B. and Jacques A. G. (1938) The Slow Hydrolysis of Ferric Chloride in Dilute
496 Solutions-II. The Change in Hydrogen Ion Concentration. J. Am. Chem. Soc. 60, 1215-
497 1225.
498 Liang, D.T. and Readey, D.W. (1987) Dissolution Kinetics of Cryalline and Amorphous Silica in
499 Hydrofluoric-Hydrochloric Acid Mixtures. Journal of American Ceramic Society, 70(8),
500 570-77.
501 C. Ma, H. C. Connolly, Jr., J. R. Beckett, O. Tschauner, G. R. Rossman, A. R. Kampf, T. J.
502 Zega, S. A. Sweeney Smith, D. L. Schrader, Brearleyite, $Ca_{12}Al_{14}O_{32}Cl_2$, a new mineral from the
503 NWA 1934 meteorite, Am Min. 96, 1199 (2011)
504 Malunda, J.J. (2000) Dissolution of Synthetic Strengite ($FePO_4 \cdot 2H_2O$) and Synthetic Variscite
505 ($AlPO_4 \cdot 2H_2O$) as Functions of pH and Citrate Level. (Doctoral dissertation). Retrieved
506 from UMI Microform 9980524.

Morris, R. V., Klingelhöfer, G., Schröder, C., Rodionov, D.S., Yen, A., Ming, D.W., de Souza Jr., P.A., Fleischer, I., Wdowiak, T., Gellert, R., Bernhardt, B., Evlanov, E.N., Zubkov, B., Foh, J., Bonnes, U., Kankeleit, E., Gütlich, P., Renz, F., Squyres, S.W., and Arvidson, R.E. (2006), Mössbauer Mineralogy of Rock, Soil, and Dust at Gusev Crater, Mars: Spirit's Journey Through Weakly Altered Olivine Basalt on the Plains and Pervasively Altered Basalt in the Columbia Hills. Journal of Geophysical Research**,** 111**,** E02S13, doi:10.1029/2005JE002584/

Morris, R.V., Ming, D.W., Blake, D.F., Vaniman, D.T., Bish, D.L., Chipera, S.J., Downs, R.T., Gellert, R., Treiman, A.H., Yen, A.S., Achilles, C.N., Anderson, R.C., Bristow, T.F., Crisp, J.A., Marais, D.J.D., Farmer, J.D., Grotzinger, J.P., Leshin, L.A., McAdam, A.C., Morookian, J.M., Morrison, S.M., Rampe, E.B., Sarrazin, P.C., Spanovich, N., Stolper, E.M., and Team, M.S. (2013) The amorphous component in martian basaltic soil in global perspective from MSL and MER missions. Lunar and Planetary Science Conference XXXIV, p. Abstract # 1653, Houston Texas.

Murphy, J., and Riley, J.P. (1962) A modified single solution method for the determination of phosphate in natural waters: Analytica Chimica Acta,. 27, 31-36.

Parkhurst, D.L., and Appelo, C.A.J. (1999) User's guide to PHREEQC (ver. 2)—A computer program for speciation, batch-reaction, one-dimensional transport, and inverse geochemical calculations. USGeol. Surv. Water- Resources Invest. Rept., 99–4259.

Perkin-Elmer Corporation (1964) Analytical Methods for Atomic Absorption Spectrophotometry, Analytical Methods for Atomic Absorption Spectrophotometry.

Putnis, A. (2009) Mineral Replacement Reactions. Reviews in Mineralogy and Geochemistry, 70, 87-124.

Roncal-Herreo, T., Rodriguez-Blanco, J.D., Benning, L.G., and Oelkers, E.H. (2009) Precipitation of Iron and Aluminum Phosphates Directly from Aqueous Solution as a Function of Temperature from 50 to 200°C: Crystal Growth and Design Article, 9, 5197-5205.

Roncal-Herrero, T. and Oelkers, E.H. (2011) Does Variscite Control Phosphate Availability in Acidic Natural Waters? An Experimental Study of Variscite Dissolution Rates. Geochimica et Cosmoshimica Acta, 75**,** 416-426.

Ruiz-Agudo, E., Putnis, C.V., Rodriguez-Navarro, C., Putnis, A. (2012) Mechanism of Leached Layer Formation During Chemical Weathering of Silicate Minerals. Geology, 40, 10, 947-950.

Siever, R. and Woodford, N. (1979) Dissolution Kinetics and the Weathering of Mafic Minerals. Geochimica et Cosmoshimica Acta, 43, 717-724.

Squyres, S.W., Knoll, A.H., Arvidson, R.E., Clark, B.C., Grotzinger, J.P., Jolliff, B.L., McLennan, S.M., Tosca, N., Bell III, J.F., Calvin, WL.M., Farrand, W.H., Glotch, T.D. Golombek, M.P., Herkenhoff, K.E., Johnson, J.R., Klingelhöfer, G., McSween, H.Y., and Yen, A.S. (2006) Two Years at Meridiani Planum: Results from the Opportunity Rover. Science, 313**,** 1403-1407.

Taxer, K. and Bartl, H. (2004) On the Dimorphy Between the Variscite and Clinovariscite Group: Refined Finestructural Relationship of Strengite and Clinostrengite, $Fe(PO_4)\cdot 2H_2O$. Crystal Research Technology, 39, 12, 1080-1088.

Tosca, N.J. and Knoll, A.H (2009) Juvenile chemical sediments and the long term persistence of water at the surface of Mars. Earth and Planetary Science Letters, v. 286, 379-386.

Vaniman, D.T., Bish, D.L., Ming, D.W., Bristow, T.F., Morris, R.V., Blake, D.F., Chipera, S.J., Morrison, S.M., Treiman, A.H., Rampe, E.B., Rice, M., Achilles, C.N., Grotzinger, J.P., McLennan, S.M., Williams, J., Bell, J.F., Newsom, H.E., Downs, R.T., Maurice, S., Sarrazin, P., Yen, A.S., Morookian, J.M., Farmer, J.D., Stack, K., Milliken, R.E., Ehlmann, B.L., Sumner, D.Y., Berger, G., Crisp, J.A., Hurowitz, J.A., Anderson, R., Des Marais, D.J., Stolper, E.M., Edgett, K.S., Gupta, S., Spanovich, N., and Team, M.S. (2014) Mineralogy of a Mudstone at Yellowknife Bay, Gale Crater, Mars. Science, 343(6169).

Viers, J., Dupre´, B., Polve, M., Schott, J., Dandurand, J.-L., and Braun, J.-J., (1997) Chemical weathering in the drainage basin of a tropical watershed (Nsimi-Zoetele site, Cameroon): comparison between organic-poor and organic-rich waters: Chemical Geology, v. 140, 181–206, doi:10.1016/S0009-2541(97)00048-X.

Weissbart, E.J., and Rimstidt, J.D. (2000) Wollastonite: Incongruent Dissolution and Leached Layer Formation. Geochimica et Cosmoshimica Acta, 64, 23, 4007-4016.

White, A.F and Brantley, S.L. (1995) The Effect of Time on the Weathering of Silicate Minerals: Why do Weathering rates Differ in the Laboratory and Field? Chemical Geology, 202, 479-506.

Zhang, M. Alva, A.K., Li, Y.C., Calvert, D.V. (2001) Aluminum and Iron Fractions Affecting Phosphorus Solubility and Reactions in Selected Sandy Soils. Soil Science, 166**,** 12.

Figure Captions:

Figure 1. (A) Schematic image of flow-through reactor based on Weissbart and Rimstidt (2000). Solution is pumped from the input reservoir using a peristaltic pump up through a 0.45 micron filter. The reactor is agitated atop a shaker plate at 150 rpm, and then solution is filtered (0.45 μm filter) before entering a collection vessel for analyses. (B) Enlarged schematic image of reactor showing flow of fluid up through sample suspended on the filter. The filter is being held in place by an acrylic sleeve and effluent solution flowing out is filtered before being collected in a vessel for analyses.

Figure 2. Representative results of dissolution of amorphous Al-phosphate (pH 2.5) (a) Flow rate (mol/min), (b) output pH (c). Al (mM) and (d) P (mM) versus time. Boxes indicate steady state conditions defined as described in text.

Figure 3. Aqueous Fe: P ratio (mM) for each dissolution experiment of amorphous Fe-phosphate (a) pH = 3 (b) pH = 2.5 (c) pH = 2 and (d) pH = 1. The solid horizontal line represents the ratio of Fe: P in the amorphous Fe phosphate. Results indicate non-stoichiometric dissolution of amorphous Fe-phosphate at higher pH with concentrations approaching stoichiometric release as pH decreases.

Figure 4. Aqueous Al: P ratio (mM) for each dissolution experiment of amorphous Al- phosphate at (a) pH = 3 (b) pH = 2.5 (c) pH = 2 and (d) pH = 1. The solid horizontal line represents the ratio of Al: P in the amorphous Al phosphate. Results indicate non-stoichiometric dissolution of amorphous Al-phosphate initially, which in all cases achieve stoichiometric dissolution by steady state conditions.

Figure 5. Micrographs of nanoporous amorphous Al-phosphate taken by Field-Emission Scanning Electron Microscopy (FE-SEM). (a) 24 hour synthesized amorphous Al-phosphate at 100nm magnification with particles sizes ~ 45 to 64nm in diameter, (b) 24 hour synthesis of amorphous Al-phosphate zoomed out to 1μm, exhibiting aggregates of particles within clusters, (c) 24 hour reacted amorphous Al-phosphate material magnified to 100nm, demonstrating particle sizes similar to those of the unreacted, but with slightly smaller diameters. (d) Aggregate of unreacted amorphous Al-phosphate synthesized at 24 hours.

Figure 6. Micrographs of nanoporous amorphous Fe-phosphate taken by Field-Emission Scanning Electron Microscopy (FE-SEM), charging was present on material surfaces causing interference of images. (a) and (b) 24 hour synthesized amorphous Fe-phosphate at

610 100nm magnification with particles sizes ~ 26 to 100nm in diameter, (c) 24 hour reacted
611 amorphous Fe-phosphate material magnified to 100nm, demonstrating particle sizes similar
612 to those of the unreacted, but slightly smaller diameters in some instances, aggregates of
613 reacted material exhibit potentially less porosity than unreacted material. (d) Aggregate of
614 unreacted amorphous Fe-phosphate synthesized at 24 hours.
615
616 Figures 7a-d. Optical images of reacted and unreacted amorphous iron-phosphate (a) and
617 (b) Reacted 24 hour amorphous iron-phosphate mounted in epoxy and impregnated. Interior
618 material is opaque and whitish surrounded by a reddish-brown rim, potentially iron
619 oxyhydroxides. (c) and (d) unreacted 24 hour synthesized amorphous iron-phosphate
620 mounted in epoxy and impregnated. Material consists of mainly a translucent reddish color
621 with small dark inclusions
622
623 Figure 8. Synchrotron diffraction data of reacted and unreacted phosphate collected with 25
624 keV energy and 10-15 μm lateral spatial resolution. Clearly, the amorphous diffraction
625 features of reacted and unreacted phosphate are indistinguishable within the examined Q-
626 range. Within this range variation in the amorphous diffraction signal was found in reacted
627 and unreacted material The unreacted phosphate contains a permille-fraction of micro-
628 crystalline FeOOH. Figure 8 insert. The diffractogram of reacted phosphate was
629 subtracted from the diffractogram of unreacted phosphate, thus removing most of the
630 amorphous diffraction signal for the unreacted material. The micro-crystalline diffraction
631 features are clearly visible. We show the calculated diffraction patterns of goethite and
632 bernalite for comparison. We note that with increasing angle the signal is somewhat

633 suppressed from the diffraction image processing and calculated and observed intensities do
634 not fully match.
635
636 Figure 9. Fe K edge XANES from 7100 to 7400 eV (inset showing the region from 7100 to
637 7120 eV). The XANES spectra indicate that the unreacted and reacted amorphous Fe
638 phosphate are very similar. The absence of a shift in the position of the main edge indicates
639 that the valence of Fe has remained unchanged during the reaction, expected for dissolution
640 of a ferric phosphate under oxidizing conditions. The much higher intensity of the white
641 line relative to literature data for tetrahedrally coordinated crystalline $FePO_4$ [Deb et al.
642 2005] is consistent with the presence of octahedrally coordinated Fe^{3+} in our amorphous
643 materials, although the white line is less intense than in the octahedrally coordinated
644 triphyllite [Deb et al. 2005]. We therefore interpret that the XANES spectra of these
645 amorphous Fe phosphates indicate that both octahedrally and tetrahedrally coordinated Fe^{3+}
646 are abundant, with some indication for a gradual progression in the crystallization of the
647 amorphous phosphate to strengite. This result is consistent with the detection of the
648 nanocrystalline strengite by TEM.
649
650 Figure 10 Dissolution rates of amorphous Al- and Fe-phosphates versus pH indicate that Al-
651 phosphates dissolve more rapidly than amorphous Fe-phosphates, which may be due to
652 precipitation of Fe oxyhydroxides. Amorphous Al-phosphates measured in this study are
653 also faster than the crystalline Al phosphate variscite. Lines represent the rate laws
654 calculated as described in the text.
655

Table 1
Summary of experimental conditions for the dissolution of amorphous Al-phosphates.

Material	inlet pH	outlet pH*	m_i (g)[β]	m_f (g)[β]	FR (ml/min)[¥]	BET SA ($cm^2 g^{-1}$)[£]	conc. Al (mM)*	conc. P (mM)*	Al:P[Φ]	Dissolution rate ($mol\ cm^{-2} s^{-1}$) Based on Al[δ]	Based on P[δ]
amorphous Al-phosphate	3.00	3.42	1.0002	0.2571	0.0463	771550	0.387	0.376	1.03	$1.509 \times 10^{-15} \pm 1.032 \times 10^{-16}$	$1.463 \times 10^{-15} \pm 6.115 \times 10^{-17}$
amorphous Al-phosphate	2.50	3.12	2.0001	0.1517	0.0468	771550	2.34	2.40	0.978	$1.558 \times 10^{-14} \pm 5.981 \times 10^{-16}$	$1.599 \times 10^{-14} \pm 6.101 \times 10^{-16}$
amorphous Al-phosphate	2.00	2.73	2.5003	0.109	0.0395	771550	9.19	9.96	0.922	$7.187 \times 10^{-14} \pm 4.066 \times 10^{-15}$	$7.792 \times 10^{-14} \pm 3.528 \times 10^{-15}$
amorphous Al-phosphate	1.02	2.28	3.0019	-	0.03	771550	193	204	0.962	[δ]	[δ]

[δ] Dissolution rates of amorphous Al- phosphates determined from steady-state concentrations and normalized to final mass.
[β] (mi) and (mf) refer to the initial and final mass of material used in flow-through dissolution experiment.
[£] BET SA refers to the initial measured specific surface area
[¥] (FR) represents the solution flow-rate
*Outlet pH, flow rate (FR) and concentrations (conc.) are based on the average of four consecutive steady state data points.
[ο] Material had completely dissolved by the end of the experiment, therefore no dissolution rates were calculated, although stoichiometry was.
[Φ] Al:P concentration ratios demonstrating stoichiometric dissolution.

Table 2
Summary of experimental conditions for the dissolution of amorphous Fe-phosphates.

Material	inlet pH	outlet pH*	m_i (g)[β]	m_f (g)[β]	FR (ml/min)[¥]	BET SA ($cm^2 g^{-1}$)[£]	conc. Fe (mM)*	conc. P (mM)*	Fe:P	Dissolution rate ($mol\ cm^{-2} s^{-1}$) Based on Fe[θ]	Based on P[θ]
amorphous Fe-phosphate	3.00	2.99	1.0003	0.5745	0.0606	1219128	0.00575207	0.0371	0.155	$8.289 \times 10^{-18} \pm 4.844 \times 10^{-19}$	$5.353 \times 10^{-17} \pm 3.044 \times 10^{-18}$
amorphous Fe-phosphate	2.50	2.48	1.999	1.1825	0.0592	1219128	0.0402608	0.0655	0.615	$2.758 \times 10^{-17} \pm 2.849 \times 10^{-18}$	$4.483 \times 10^{-17} \pm 3.949 \times 10^{-18}$
amorphous Fe-phosphate	2.00	2.10	1.0002	0.5114	0.0479	1219128	0.131732	0.17	0.774	$1.688 \times 10^{-16} \pm 9.128 \times 10^{-18}$	$2.179 \times 10^{-16} \pm 1.034 \times 10^{-17}$
amorphous Fe-phosphate	1.02	1.22	2.9996	-	0.0414	1219128	64.2933	73.7	0.876	[δ]	[δ]

[θ] Dissolution rates of amorphous Fe- phosphates determined from steady-state concentrations and normalized to final mass.
[β] (mi) and (mf) refer to the initial and final mass of material used in flow-through dissolution experiment.
[£] BET SA refers to the initial measured specific surface area
[¥] (FR) represents the solution flow-rate.
*Outlet pH, flow rate (FR) and concentrations (conc.) are based on the average of four consecutive steady state data points.
[δ] Material had completely dissolved by the end of the experiment, therefore no dissolution rates were calculated, although stoichiometry was.
[ϕ] Fe:P concentration ratios demonstrating non-stoichiometric dissolution.

Table 3
Mineral solubility constants.

Mineral Name	Dissolution equation	log *Ksp*
10nm Goethite [θ]	$FeOOH + 3\ H^+ = Fe^{3+} + 2\ H_2O$	1.711
10nm Hematite [ᵾ]	$Fe_2O_3 + 6\ H^+ = 2\ Fe^{3+} + 3\ H_2O$	2.241
10nm Maghemite [ᵾ]	$Fe_2O_3 + 6\ H^+ = 2\ Fe^{3+} + 3\ H_2O$	4.1
Ferrihydrite [a]	$Fe(OH)_3 + 3\ H^+ = + Fe^{3+} + 3\ H_2O$	5.6556
Goethite [ᵝ]	$FeOOH + 3\ H^+ = + Fe^{3+} + 2\ H_2O$	0.5345
Hematite [ᵝ]	$Fe_2O_3 + 6\ H^+ = + 2\ Fe^{3+} + 3\ H_2O$	0.1086
Maghemite [a]	$Fe_2O_3 + 6\ H^+ = 2\ Fe^{+3} + 3\ H_2O$	2.18
Strengite [ᵝ]	$FePO_4(H_2O)_2 = Fe^{3+} + PO_4^{3-} + 2\ H_2O$	-26
Vivianite [ᵝ]	$Fe_3(PO_4)2{:}8H_2O + 2\ H^+ = + 2\ HPO_4^- + 3\ Fe^{2+} + 8\ H_2O$	-4.7237
Gibbsite [ᵝ]	$Al(OH)_3 + 3\ H^+ = + Al^{3+} + 3\ H_2O$	7.756
Variscite [£]	$AlPO_4(H_2O)_2 = Al^{3+} + PO_4^{3-} + 2\ H_2O$	-21

[θ] Log *Ksp* and dissolution equation from by Elwood-Madden et al., [2009]

[ᵝ] Log *Ksp* and dissolution equation from the Lawrence Livermore National Laboratory (llnl) database.

[£] Log *Ksp* and dissolution equation from Roncal-Herrero et al. [2009]

Table 4
Saturation indices for the average of each steady state condition.

Material	inlet pH	outlet pH	T (°C)	SI[a] Strengite	Hematite	Goethite	Vivianite	Maghemite	Ferrihydrite	10nm Hematite	10nm Goethite	10nm Maghemite
Amorphous Fe-phosphate	1.02	1.22	20	-4.4	-15.7	-8.33	-15.32	-17.77	-13.45	-17.83	-9.51	-19.69
Amorphous Fe-phosphate	2.00	2.1	20	-6.4	-13.85	-7.4	-21.04	-15.92	-12.52	-15.98	-8.58	-17.84
Amorphous Fe-phosphate	2.50	2.48	20	-6.49	-12.4	-6.68	-21.5	-14.47	-11.8	-14.53	-7.86	-16.39
Amorphous Fe-phosphate	3.00	2.99	20	-6.51	-11.04	-6	-22.52	-13.11	-11.12	-13.17	-7.17	-15.03

[a] Saturation index for average solutions determined by PHREEQ-C modeling using log *Ksp* from table 1. For saturation index of each concentration refer to the appendices.

Table 5
Saturation indices for the average of each steady state condition.

Experiment ID	inlet pH	outlet pH	T (°C)	SI[6]	
				Variscite	Gibbsite
Amorphous Al-phosphate	1.02	2.28	20	1.08	-7.44
Amorphous Al-phosphate	2.00	2.73	20	2.12	-2.12
Amorphous Al-phosphate	2.50	3.12	20	1.95	-1.42
Amorphous Al-phosphate	3.00	3.42	20	1.18	-1.1

[6]Saturation index for average solutions determined by PHREEQ-C modeling using log *Ksp* from table 1. For saturation index of each concentration refer to the appendices.

741

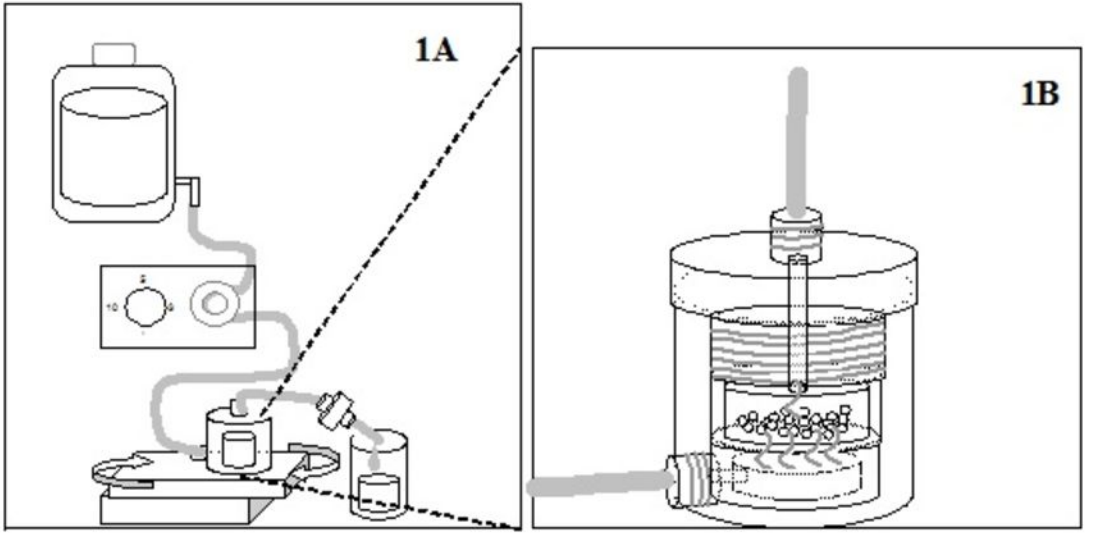
1A
1B

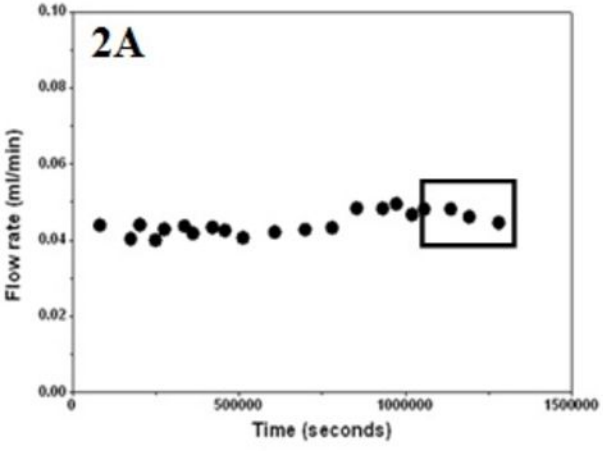
2A
Flow rate (ml/min)
0.10
0.08
0.06
0.04
0.02
0.00
0
500000
1000000
1500000
Time (seconds)

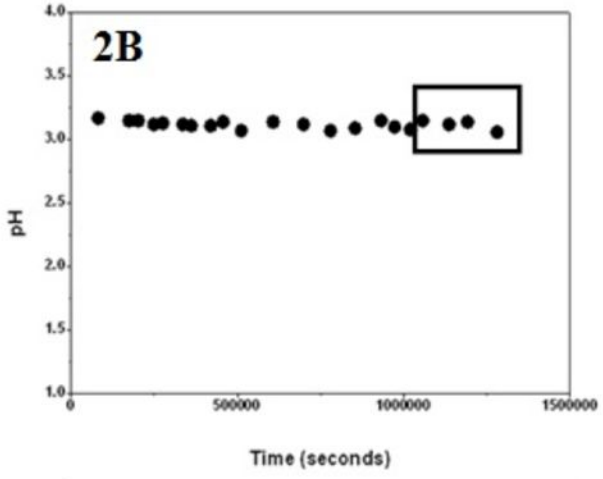
2B
pH
4.0
3.5
3.0
2.5
2.0
1.5
1.0
0
500000
1000000
1500000
Time (seconds)

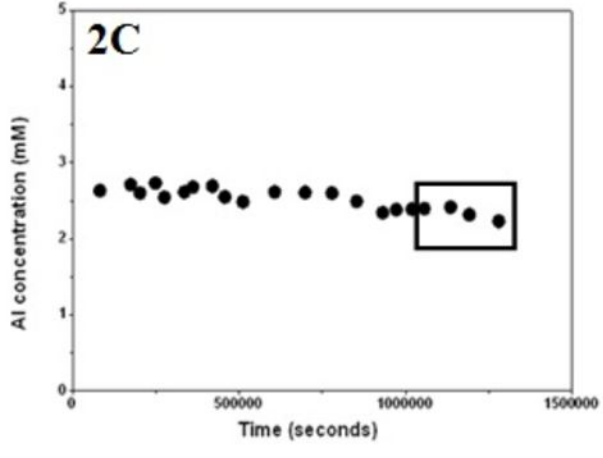
2C
Al concentration (mM)
5
4
3
2
1
0
0
500000
1000000
1500000
Time (seconds)

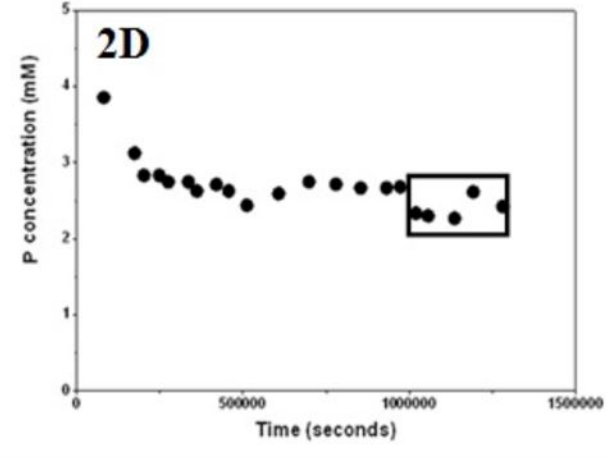
2D
P concentration (mM)
5
4
3
2
1
0
0
500000
1000000
1500000
Time (seconds)

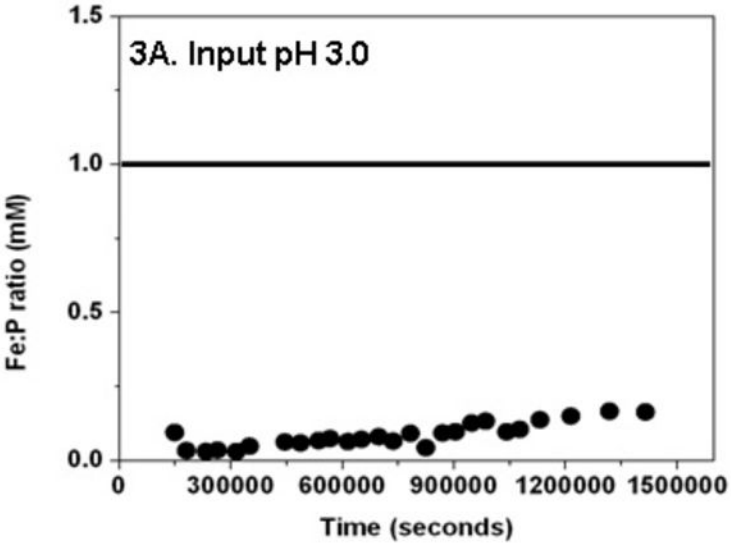
3A. Input pH 3.0
Fe:P ratio (mM)
Time (seconds)
0.0
0.5
1.0
1.5
0
300000
600000
900000
1200000
1500000

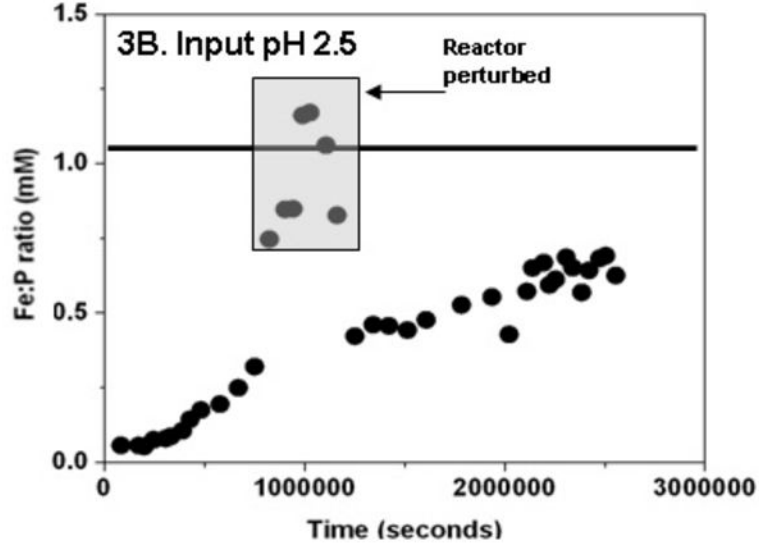
3B. Input pH 2.5
Reactor perturbed
Fe:P ratio (mM)
Time (seconds)
0.0
0.5
1.0
1.5
0
1000000
2000000
3000000

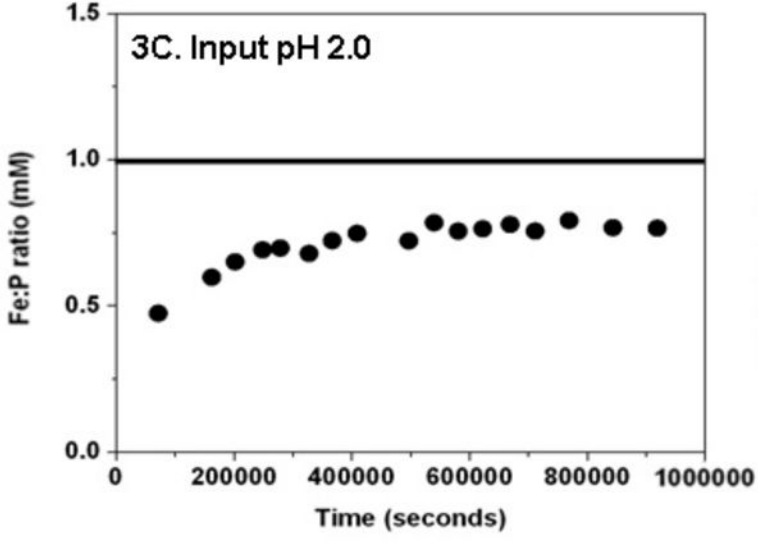
3C. Input pH 2.0
Fe:P ratio (mM)
Time (seconds)
0.0
0.5
1.0
1.5
0
200000
400000
600000
800000
1000000

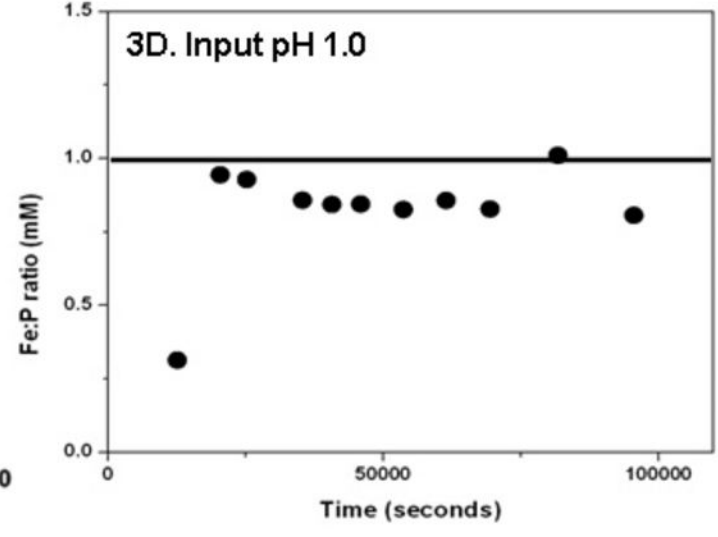
3D. Input pH 1.0
Fe:P ratio (mM)
Time (seconds)
0.0
0.5
1.0
1.5
0
50000
100000

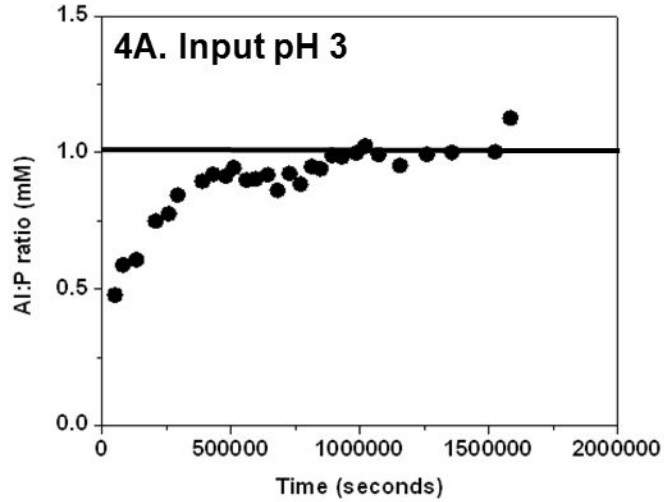
4A. Input pH 3
Al:P ratio (mM)
1.5
1.0
0.5
0.0
0
500000
1000000
1500000
2000000
Time (seconds)

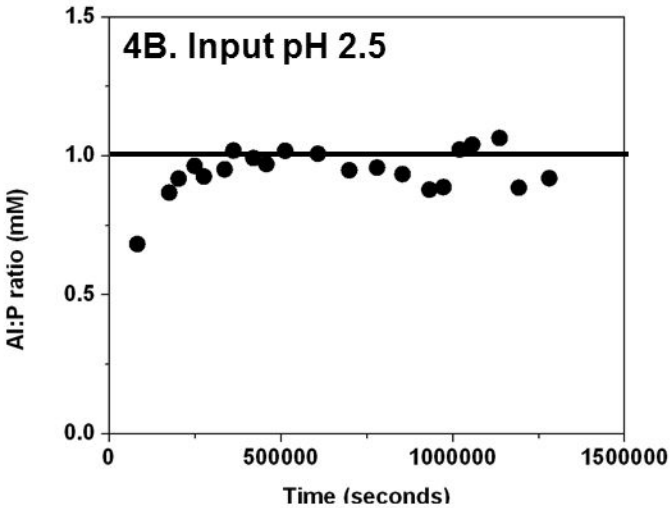
4B. Input pH 2.5
Al:P ratio (mM)
1.5
1.0
0.5
0.0
0
500000
1000000
1500000
Time (seconds)

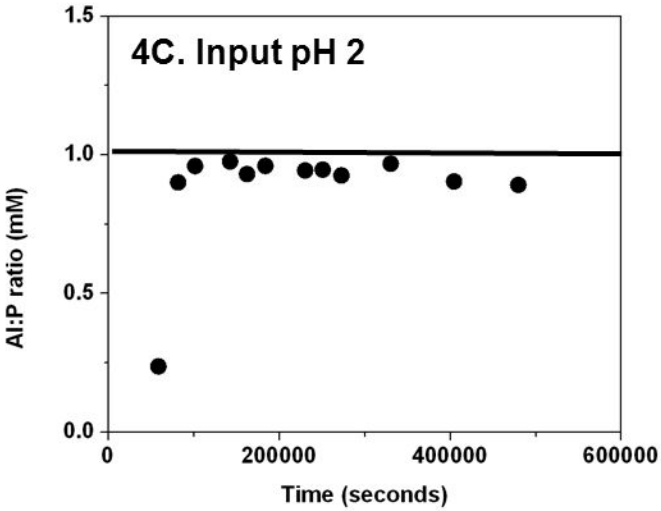
4C. Input pH 2
Al:P ratio (mM)
1.5
1.0
0.5
0.0
0
200000
400000
600000
Time (seconds)

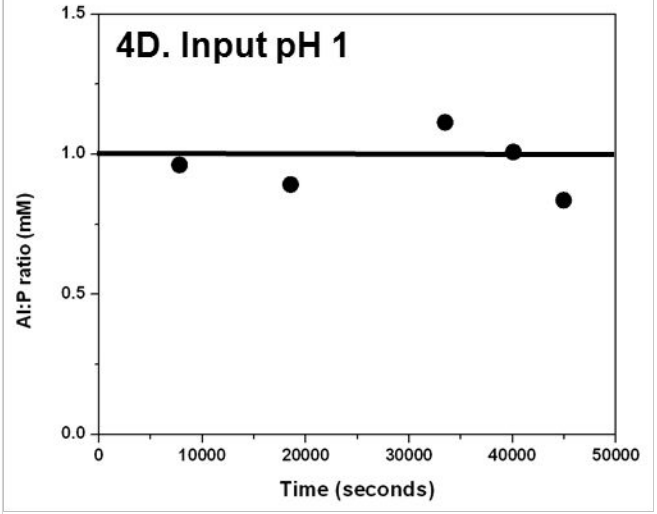
4D. Input pH 1
Al:P ratio (mM)
1.5
1.0
0.5
0.0
0
10000
20000
30000
40000
50000
Time (seconds)

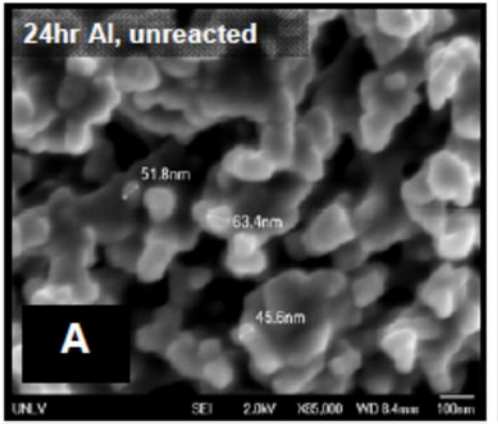
24hr Al, unreacted
51.8nm
63.4nm
45.6nm
A
UNLV SEI 2.0kV X85,000 WD 8.4mm 100nm

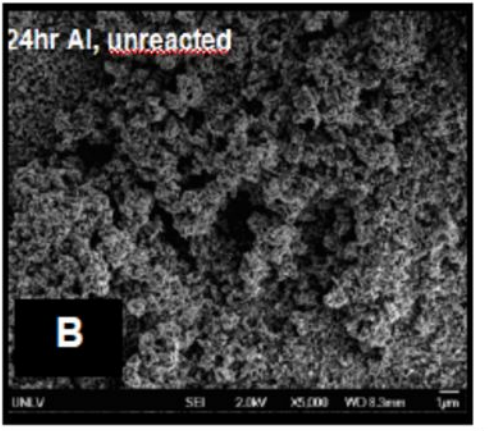
24hr Al, unreacted
B
UNLV SEI 2.0kV X5,000 WD 8.3mm 1μm

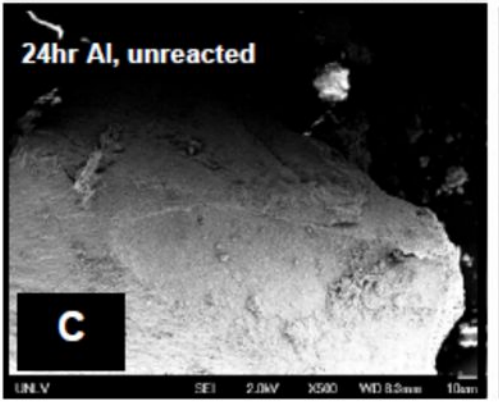
24hr Al, unreacted
C
UNLV SEI 2.0kV X500 WD 8.5mm 10μm

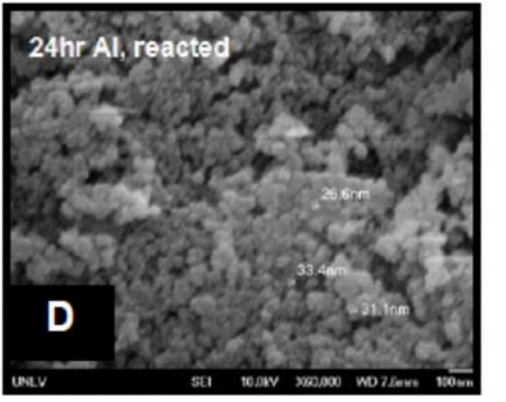
24hr Al, reacted
26.6nm
33.4nm
31.1nm
D
UNLV SEI 10.0kV X60,000 WD 7.6mm 100nm

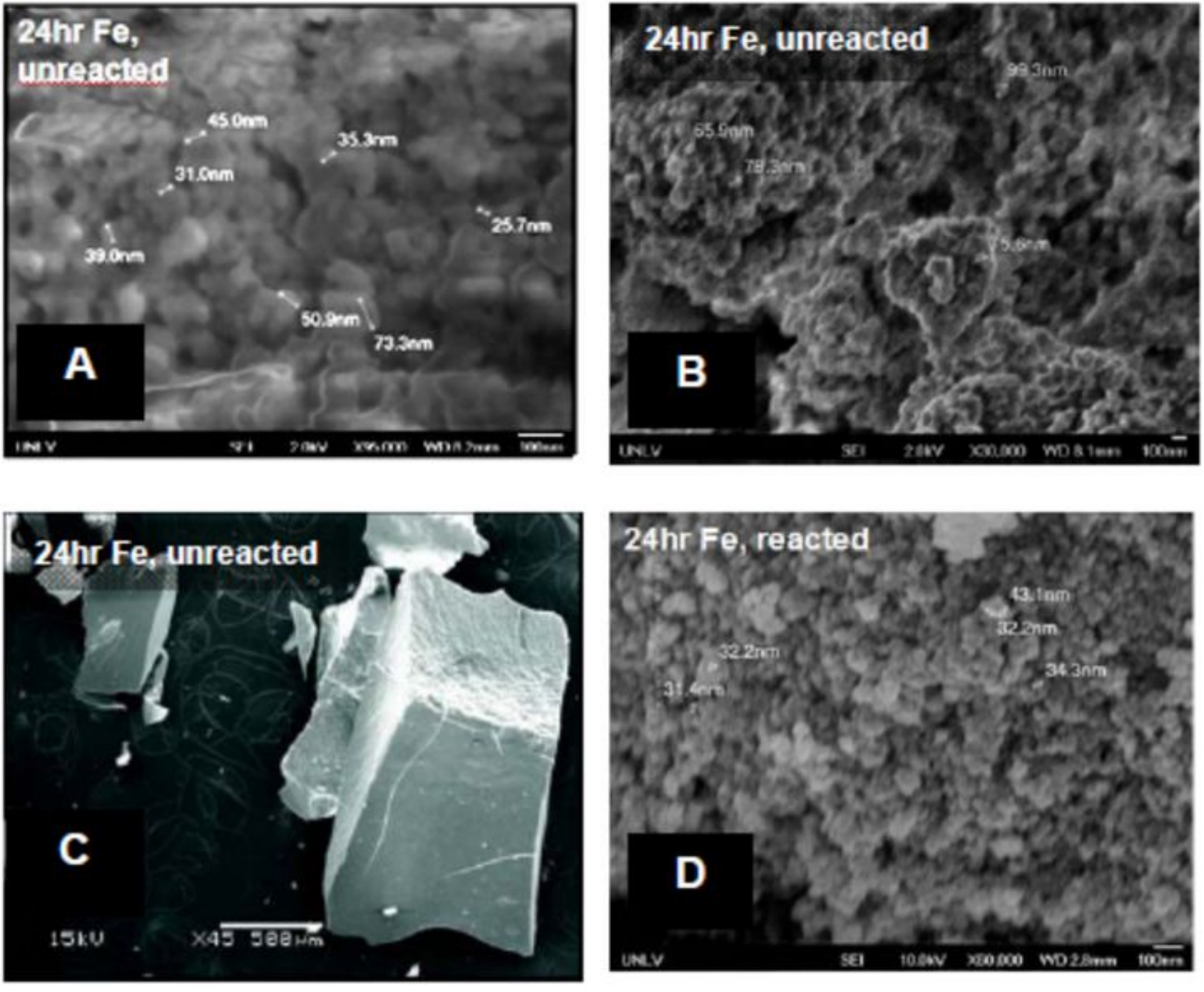
24hr Fe, unreacted
45.0nm
35.3nm
31.0nm
25.7nm
39.0nm
50.9nm
73.3nm
A
24hr Fe, unreacted
99.3nm
65.9nm
78.3nm
5.6nm
B
24hr Fe, unreacted
C
15kV
X45
24hr Fe, reacted
43.1nm
32.2nm
32.2nm
34.3nm
31.4nm
D

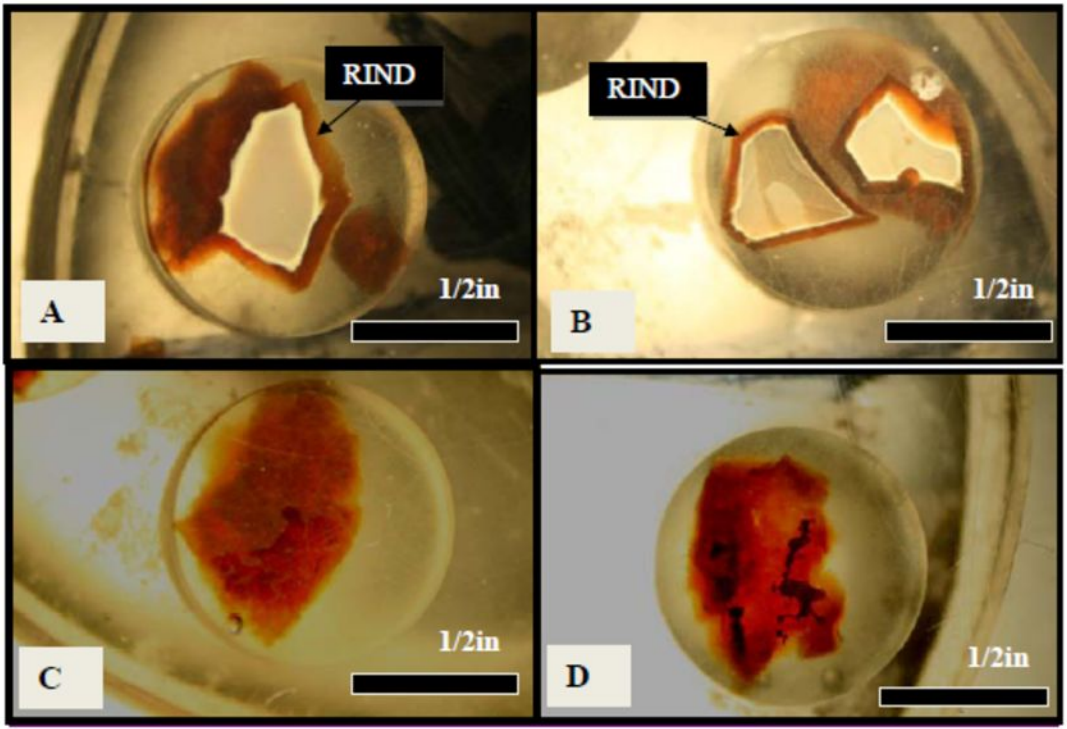
RIND
1/2in
A
RIND
1/2in
B
1/2in
C
1/2in
D

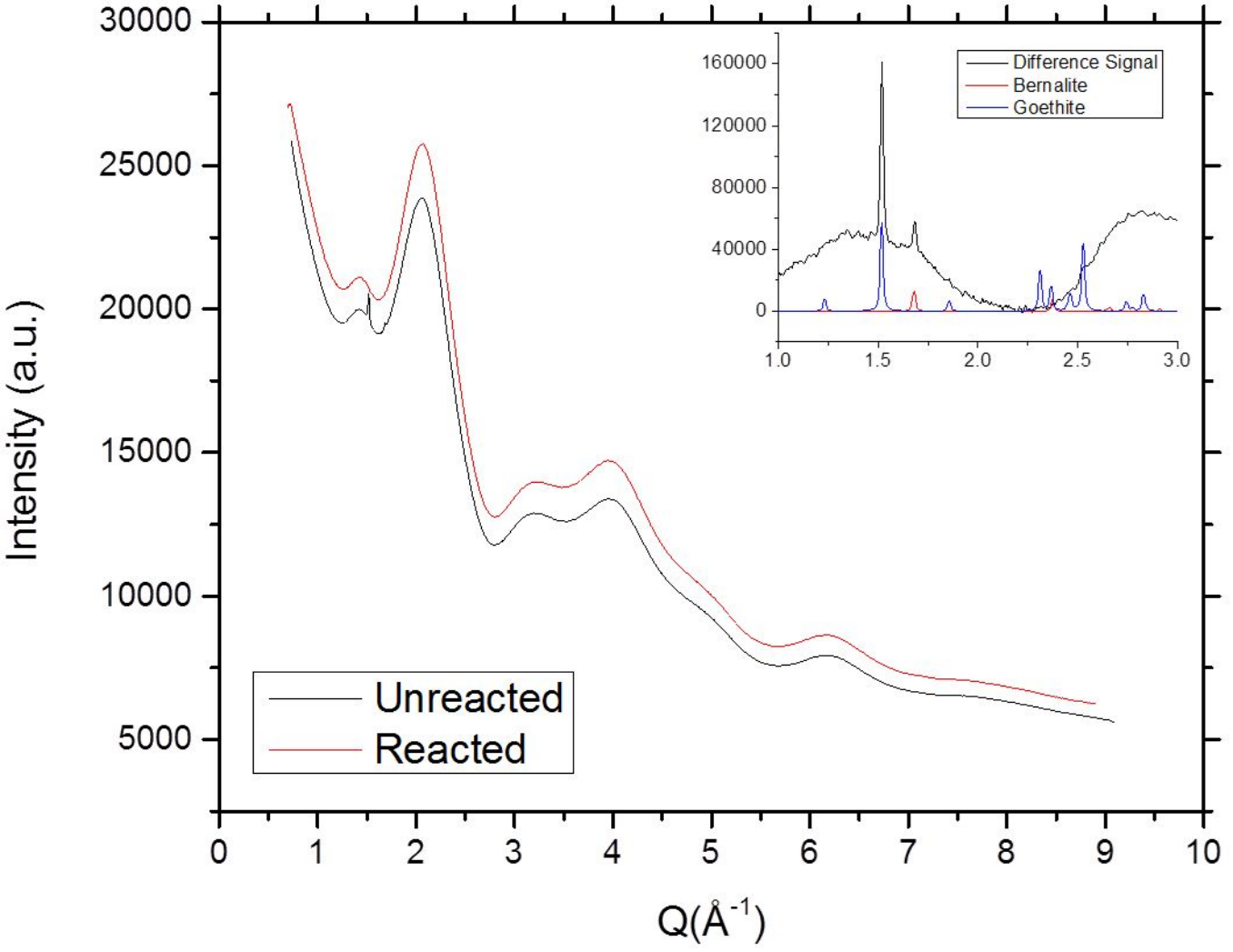
Intensity (a.u.)
Q(Å^{-1})
Unreacted
Reacted
Difference Signal
Bernalite
Goethite

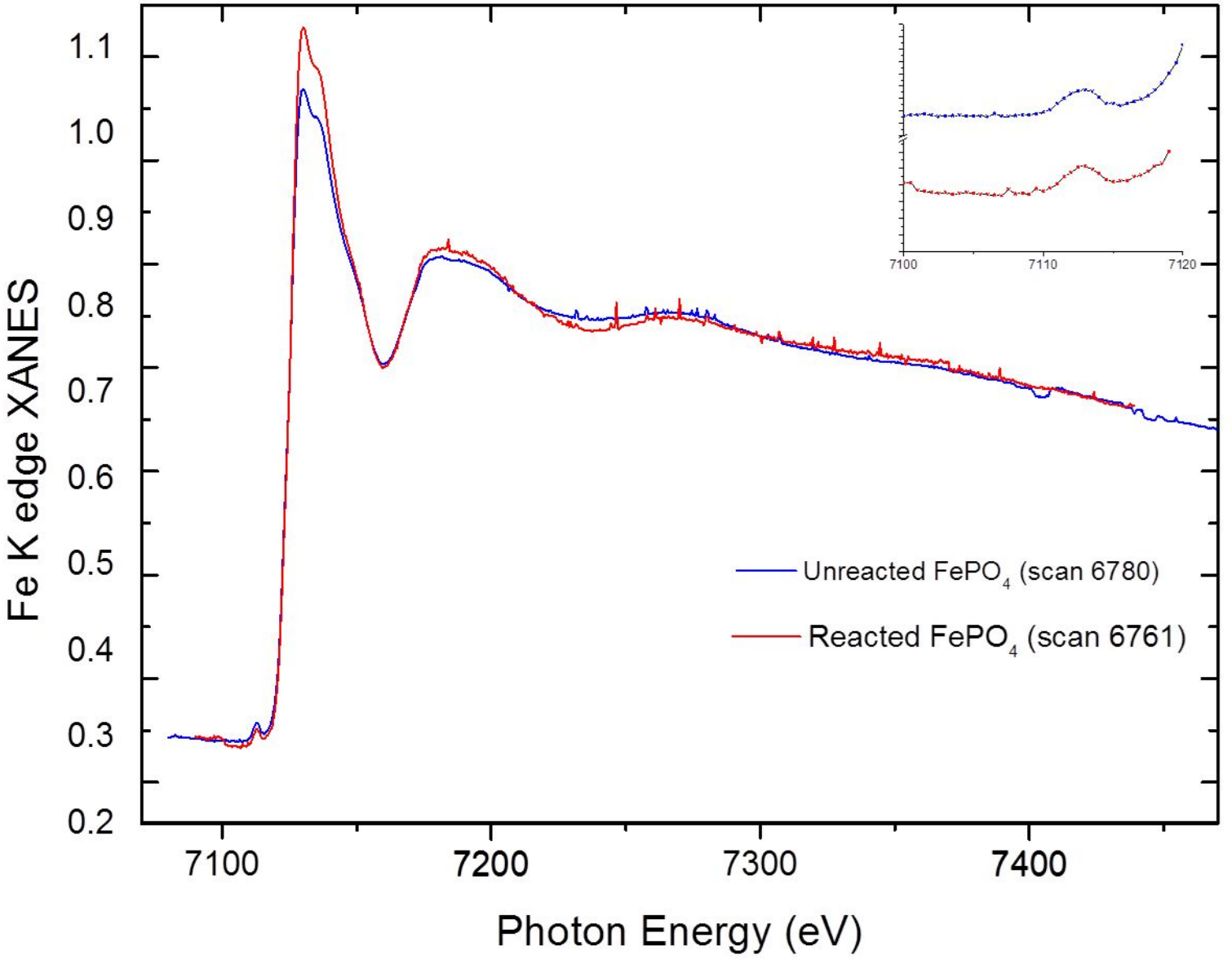
Fe K edge XANES
1.1
1.0
0.9
0.8
0.7
0.6
0.5
0.4
0.3
0.2
7100
7200
7300
7400
Photon Energy (eV)
Unreacted FePO4 (scan 6780)
Reacted FePO4 (scan 6761)
7100
7110
7120

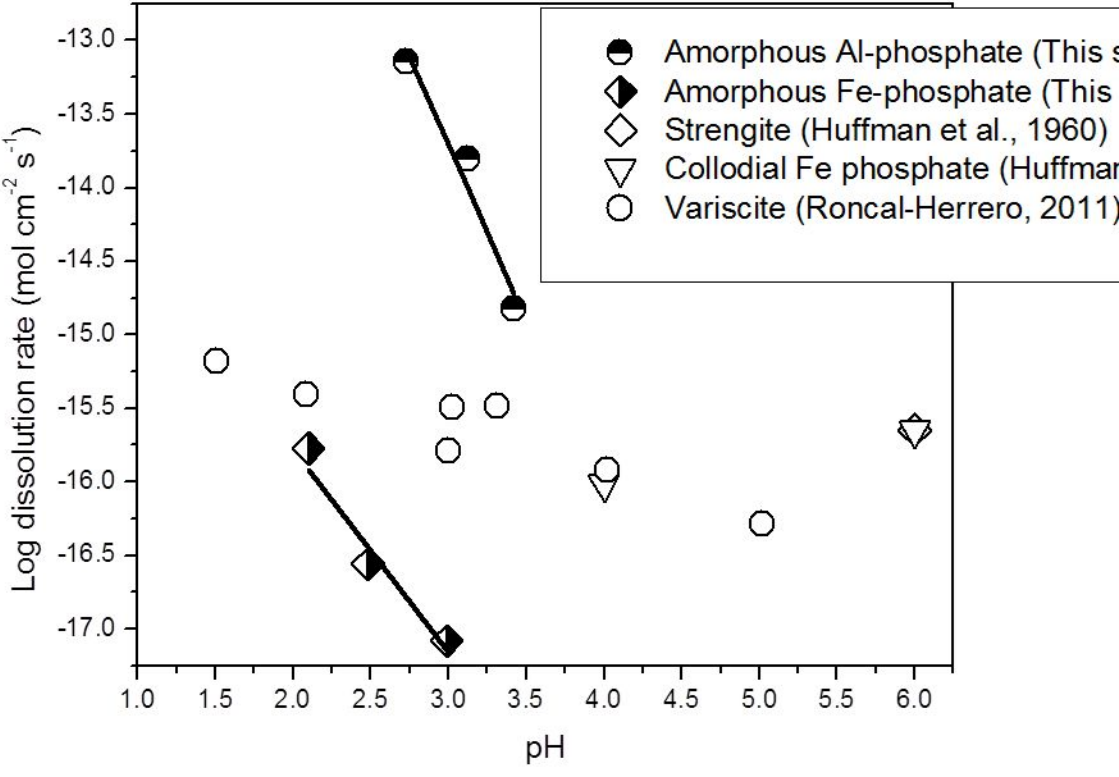
Amorphous Al-phosphate (This s
Amorphous Fe-phosphate (This
Strengite (Huffman et al., 1960)
Collodial Fe phosphate (Huffman
Variscite (Roncal-Herrero, 2011)
Log dissolution rate (mol cm-2 s-1)
-13.0
-13.5
-14.0
-14.5
-15.0
-15.5
-16.0
-16.5
-17.0
1.0
1.5
2.0
2.5
3.0
3.5
4.0
4.5
5.0
5.5
6.0
pH